Change in the magnitude and mechanisms of global temperature variability with warming

Patrick T. Brown[1,*], **Yi Ming**[2], **Wenhong Li**[3], and **Spencer A. Hill**[4,5]

[1]Department of Global Ecology, Carnegie Institution for Science, Stanford, California

[2]Geophysical Fluid Dynamics Laboratory/NOAA, Princeton, New Jersey

[3]Earth and Ocean Sciences, Nicholas School of the Environment, Duke University, Durham, North Carolina

[4]Department of Atmospheric and Oceanic Sciences, University of California, Los Angeles, California

[5]Division of Geological and Planetary Sciences, California Institute of Technology, Pasadena, California

Abstract

Natural unforced variability in global mean surface air temperature (GMST) can mask or exaggerate human-caused global warming, and thus a complete understanding of this variability is highly desirable. Significant progress has been made in elucidating the magnitude and physical origins of present-day unforced GMST variability, but it has remained unclear how such variability may change as the climate warms. Here we present modeling evidence that indicates that the magnitude of low-frequency GMST variability is likely to decline in a warmer climate and that its generating mechanisms may be fundamentally altered. In particular, a warmer climate results in lower albedo at high latitudes, which yields a weaker albedo feedback on unforced GMST variability. These results imply that unforced GMST variability is dependent on the background climatological conditions, and thus climate model control simulations run under perpetual preindustrial conditions may have only limited relevance for understanding the unforced GMST variability of the future.

Global mean surface air temperature (GMST) is one of the most well-recognized metrics of climate change both contemporarily as well as through deep time. On centennial timescales, positive external radiative forcings, mostly due to increased concentrations of well-mixed greenhouse gasses, are currently causing pronounced GMST warming[1]. However, unforced

GMST change, which is spontaneously generated from interactions internal to the ocean-atmosphere-land system, superimposes variability on this long-term warming that can alternatively mask or exaggerate externally forced signals for years to decades at a time[2–4]. Thus, in order to attribute past changes to human activities or to accurately predict climate change on policy-relevant decadal timescales, robust understanding of both the magnitude and mechanisms responsible for unforced GMST variability is critical.

Three principal methodologies are typically used to surmise information on the physics and statistics of contemporary unforced GMST variability: **1)** Unforced GMST variability is studied using the output of coupled atmosphere-ocean global climate models run under perpetual preindustrial boundary conditions[5–10], **2)** Unforced GMST variability is studied using observed or reconstructed datasets spanning the most recent century to approximately the past millennium[11–17], and/or **3)** Unforced GMST variability is studied in climate model experiments that incorporate historical estimates of time-varying external radiative forcings[2,9,18–21]. Such studies could be used to draw inferences about unforced GMST variability in the future if it is assumed that GMST variability is more-or-less independent of the climatological GMST. However, given that many features of the climate system are not independent of absolute temperature, it is plausible that the physics and statistics of GMST variability might not be conserved across a wide range of climatological GMST values. For example, a warmer climate will likely be characterized by changes in mean sea ice extent[22], hydrology[22], upper ocean stratification[23], and surface energy budget partitioning[24], all of which could impact GMST variability.

Previous work has emphasized changes in local surface air temperature (SAT) variability with warming[25–32] but the purpose of the present study is to examine how GMST variability may or may not change as the underlying climate warms. We perform detailed analysis on an experiment utilizing the fully-coupled GFDL CM3 climate model, and we supplement this with results from an atmosphere-only GFDL AM3 experiment as well as relevant results from Phase 5 of the Coupled Model Intercomparison Project (CMIP5)[33] archive (see Methods)

Response of GMST variability to GMST warming

First we compare approximately nine centuries of variability in the fully coupled GFDL CM3 model run under perpetual preindustrial radiative boundary conditions to variability in the same model after the climate system has equilibrated to a doubling of atmospheric CO_2 concentration (Fig. 1). The warming of the climatological GMST (+4.8K) is associated with a ~43% reduction (~9% reduction per K of GMST warming) in the temporal standard deviation of low-frequency GMST variability (identified with a 15-year lowess[34] filter; cf. blue and red lines in Fig. 1a and 1b). The reduction in variability is not specific to the definition of low-frequency timescale – it occurs on virtually all timescales longer than approximately a decade (cf. blue and red lines in Fig. 1c).

Not only is there a large change in the *magnitude* of low-frequency GMST variability between the GFDL CM3 preindustrial control and 2×CO2 runs, there is also an alteration in the geographic origin of GMST variability. Figures 1d and 1e show the local SAT regression

against low-frequency GMST variability, which highlights the regions that contribute the most to GMST variability in each run. Stippling represents "Regions of Significant Influence" (ROSIs)[5] on GMST variability, which are locations that have a statistically significant relationship between local SAT and GMST variability, have local SAT variability that tends to lead GMST variability in time, and have local SAT variability that tend to enhance the magnitude of GMST variability. In the preindustrial control run, low-frequency GMST variability (hereafter, GMST variability) is primarily associated with SAT variability over the Southern Ocean and Antarctica (Fig. 1d). In the $2\times CO_2$ run, however, the origin of GMST variability shifts to be almost exclusively Northern Hemispheric in origin (Fig. 1e). In particular, GMST variability becomes much more associated with the model's Atlantic Multidecadal Oscillation (AMO) in the $2\times CO_2$ run ($r^2=0.62$) compared to the preindustrial control run ($r^2=0.36$), even though the magnitude of AMO variability does not change between the two runs (Supplementary Fig. 1).

Mechanisms underlying the change in GMST variability

Unforced variability in GMST can result from an internally generated change in the net exchange of heat between the ocean and atmosphere[35–38] and/or from an internally generated change in Earth's top-of-atmosphere (TOA) energy budget[6,39,40]. Therefore, insight on the physical explanations for unforced GMST variability can be gained by investigating lagged regression coefficients (cross-regressions) between GMST and the net anomalous downward TOA energy flux (↓N) as well the net anomalous upward surface energy flux (↑Q) (Fig. 2).

In the preindustrial control run, positive ↓N anomalies tend to precede positive GMST anomalies in time (black solid line in Fig. 2a) and negative ↑Q anomalies tend to precede positive GMST anomalies in time (black solid line in Fig. 2c) indicating a tendency for net flow of energy from space to the ocean concurrent with unforced GMST warming events. This relationship suggests that internally generated ↓N imbalances tend to enhance GMST variability. Of the four linearly additive components of ↓N [clear-sky shortwave (↓clear SW); clear-sky longwave (↓clear LW); cloud radiative effect shortwave (↓cloud SW); cloud radiative effect longwave (↓cloud LW); see Methods], only the ↓clear LW damps GMST variability (red solid line in Fig. 2a). Both the ↓cloud LW and ↓cloud SW shortwave components enhance GMST variability, but the largest amplifying contribution comes from the ↓clear SW (blue dashed line Fig. 2a). The shortwave components of the energy budget, both at the TOA and the surface (blue dashed line in Fig. 2c), tend to *lead* GMST variability in time and thus appear to partially drive GMST perturbations in the preindustrial control run.

The spatial distribution of anomalous energy fluxes indicates that the Southern Ocean is a key region responsible for producing the ↓N variability that enhances GMST variability in the preindustrial control run. The dynamics of this Southern Ocean variability appear to be consistent with those expounded upon in previous studies[41–43]. Specifically, it has been shown that southward flowing North Atlantic Deep Water can deposit relatively warm, salty water at intermediate depths in the Southern Ocean. A large reservoir of heat can build up if convection is initially inhibited due to a relatively fresh surface layer and/or the presence of

surface sea ice that obstructs air-sea heat exchange. Eventually, stochastic forcing via wind stress or surface salinity anomalies can cause the onset of convection (represented by deepening of the mixed layer; Supplementary Fig. 4e). During convection, saltier water from mid-depth is transported to the surface where a rise in salinity occurs (Supplementary Fig. 4f). As convection continues, substantial anomalous surface heat flux from the high-latitude Southern Ocean to the atmosphere occurs (Supplementary Fig. 5b) due primarily to the sensible and latent heat flux components (Supplementary Fig. 5c and 5d). The excess energy is not damped to space locally, as a large reduction in sea ice extent causes a positive anomalous ↓clear SW flux (Supplementary Fig. 6c), especially in the summer (Supplementary Fig. 6i), and a net positive ↓N over the Southern Ocean (Supplementary Fig. 6b).

In the $2\times CO_2$ run, the relationship between GMST, ↓N, and ↑Q is fundamentally altered. Specifically, in the $2\times CO_2$ run, anomalous GMST warmth tends to be preceded for several years by negative ↓N values, in direct contrast to the preindustrial control run. This alteration of the relationship between GMST and anomalous energy flow can be traced primarily to changes in the summer half-year (Supplementary Figs. 2 and 3). In particular, the $2\times CO_2$ run experiences a large reduction in the ↓clear SW component's contribution to GMST change (cf. blue dashed line in Fig. 2a and 2b, noting that the Y-axis spans a smaller range in Fig. 2b than in Fig. 2a), which is primarily due to a reduction in its summertime magnitude (cf. blue dashed line in Supplementary Figs. 2c and 2d). This effect is also apparent in the net surface shortwave component (cf. blue dashed line in Fig. 2c and 2d and Supplementary Figs. 3c and 3d).

The $2\times CO_2$ run exhibits GMST variability that is associated with the model's AMO (Fig. 1e). This is consistent with an enhanced contribution of North Atlantic latent and sensible heat flux to GMST variability in this run (Supplementary Fig. 9c and 9d). Additionally, since shortwave cloud feedback enhances the AMO[44], the $2\times CO_2$ run is also characterized by a positive change in the contribution of ↓N to GMST variability over the North Atlantic (Fig. 3e, 3b). Despite this local increase, there is an overall reduction in the ↓N contribution to GMST variability between the preindustrial and $2\times CO_2$ runs primarily due to a reduction over the Southern Ocean (Fig. 3b). Specifically, over the Southern Ocean, climatological GMST warming is associated with a reduction in the climatological sea ice extent and associated climatological albedo (Supplementary Fig. 7c). This causes a reduced contribution of ↓clear SW (Fig. 3c) and thus ↓N to GMST variability. Seasonally, the summer half-year produces most of the radiative change (cf. Supplementary Figs. 7i and 7o) because of the vast seasonal difference in incident solar radiation at high latitudes.

Additionally, GMST warming has been shown to be associated with stratification of the Southern Ocean and a reduced propensity for the kind of sustained open-ocean convection that appeared to influence GMST variability in the preindustrial control run[23]. Indeed, the $2\times CO_2$ run shows a reduction in Southern Ocean convection (Supplementary Fig. 10e), latent heat flux (Supplementary Fig. 9c), and sensible heat flux (Supplementary Fig. 9d) associated with GMST variability.

The changes in the magnitude and mechanisms of GMST variability apparent in the GFDL CM3 model are qualitatively reproduced in aggregate results from a subset of other CMIP5 models (see Methods, Supplementary Table 1). Specifically, we find that CMIP5 models show a statistically significant (at the 90% confidence level), 26% reduction in the magnitude of GMST variability (Supplementary Fig. 11) between their preindustrial control runs and the 2200–2300 time period of their RCP8.5 runs. This amounts to a ~3% reduction in GMST variability per K of climatological GMST warming. Also, qualitatively consistent with the GFDL-CM3 model, the reduction in GMST variability largely emerges from a reduction in the high-latitude contribution to this variability (Supplementary Fig. 12a) which stems from a reduction in the ↓clear SW contribution to GMST variability (supplementary Fig. 12c). It has been shown that CMIP5 model spread in the magnitude of GMST variability primarily originates from differences in simulated variability at high latitudes[45]. Thus, a proportionately larger reduction in high-latitude variability in a warmer climate also reduces inter-model spread in GMST variability (Supplementary Fig. 11).

The CMIP5 models investigated here, however, show a large diversity in their GMST variability response to climatological GMST warming. At one end of the range, MPI-ESM-LR, bcc-cms1-1, and CCSM4 simulate ~55%, ~50% and ~44% reductions in GMST variability between their preindustrial control and RCP8.5 runs (all ~6% reduction per K of climatological GMST warming). On the other end of the continuum, the CNRM-CM5 model shows a ~7% increase in GMST variability between the two runs (~1% increase per K GMST warming). Future work is required to understand this range of model behavior.

Changes in local surface temperature variability

Previous studies have indicated that SAT variability may increase over certain locations with warming[26–32]. Therefore, it is of interest to investigate whether the noted decrease in GMST variability apparent in GFDL CM3 and the CMIP5 experiments applies uniformly to the entirety of the Earth's surface or if there is substantial spatial heterogeneity. Figure 4a shows the fractional change in local low-frequency SAT variability between the preindustrial control and $2\times CO_2$ runs of GFDL CM3. Consistent with the results above, there is a large decrease in local variability over the Arctic and Southern Oceans associated with a reduction in climatological sea ice extent. The reduction of sea ice should reduce local SAT variability both because it reduces the propensity for albedo variability but also because the open ocean represents greatly enhanced surface heat capacity compared to sea ice[32].

In contrast to the reduced SAT variability at high latitudes, a large fraction of tropical and subtropical land areas actually experience an increase in variability between the preindustrial control and $2\times CO_2$ runs. A similar effect is also seen in a supplementary model run where a free running atmosphere was forced with a uniform +4K increase in sea surface temperatures (Fig. 4c, see Methods) as well as in the CMIP5 ensemble mean (Supplementary Fig. 13a). The consistency of this effect between these different sets of experiments indicates that the enhancement of local SAT variability over some land regions is primarily driven by the climatological warming itself rather than resulting from particular changes in large-scale ocean-atmosphere-sea-ice modes of variability or in the spatial pattern of sea surface temperature warming.

In order to illuminate the first-order causes of locally increased land SAT variability, we compare mean changes in the surface energy budget between land locations in which low-frequency SAT variability increases with warming and land locations in which low-frequency SAT variability decreases with warming in the two GFDL model experiments (Fig. 4b and 4d) and in the CMIP5 runs (Supplementary Fig. 13b). In all experiments, there is little difference in climatological radiative surface energy availability ($\downarrow R_s$, see Methods) between the locations where SAT variability increases and the locations where SAT variability decreases (i.e., $\downarrow R_s$ changes similarly in Fig. 4b, $\downarrow R_s$ changes similarly in 4d and $\downarrow R_s$ changes similarly in Supplementary Fig. 13b). However, in all experiments, climatological sensible heating ($\uparrow SH$) increases more and climatological latent heating ($\uparrow LE$) increases less over locations where SAT variability increases (Fig. 4c, 4d and Supplementary Fig. 14b). This can be partially explained by moisture availability (approximated here as precipitation multiplied by the latent heat of vaporization, $\downarrow LP$), which increases less over regions where SAT variability increased. Thus, land regions where local SAT variability increased tend to be regions where moisture availability declines with warming. Over these locations, incident radiation variability is able to have a stronger influence on SAT variability, because proportionally more incident radiation is converted to sensible (rather than latent) heat flux[46]. Many low- to mid-latitude land regions should fit this description, since land amplification of warming is likely to cause an increase in aridity[24,46–48].

Discussion

We show here that the magnitude of low-frequency unforced GMST variability is substantially reduced in the GFDL CM3 climate model after a doubling of CO_2 from preindustrial levels and that the mechanisms responsible for that variability are fundamentally altered. In particular, the modes of variability primarily responsible for generating GMST variability are shifted in space, and the net flow of energy associated with unforced warming events changes from being into the climate system to out of the climate system (vice-versa for unforced cooling events). We find that a primary reason for this shift is the reduction in high-latitude surface albedo variability which results from a climatological reduction in albedo. Finally, we find that local variability over many tropical and subtropical land areas increases with global warming despite the reduction in GMST variability.

A number of caveats should be stressed with regard to this study. Reasons for caution include the attribute that the GFDL CM3 model has unusually large GMST variability in its preindustrial control run[5] as well as a $2\times CO_2$ climate sensitivity towards the upper range of the CMIP5 ensemble range[49]. Taken together, these features may indicate that the reduction of GMST variability with a doubling of CO_2 may be exaggerated in GFDL CM3 compared to reality. As discussed above, the CMIP5 models investigated here show a smaller mean change in unforced GMST variability between their preindustrial control and RCP8.5 runs (~3% per K of climatological GMST warming on average compared to ~9% per K of climatological GMST warning in GFDL-CM3). Also, climate models differ substantially in the geographic origin and generating mechanisms of their unforced GMST variability[5], and

thus changes in the generating mechanisms of GMST variability will likely vary substantially from model to model.

Thus, we emphasize that the results from GFDL CM3 model should not necessarily be interpreted as a robust quantitative forecast of future variability change. Instead the results of this study serve to demonstrate that the magnitude and mechanisms of unforced GMST variability may depend critically on the climatological GMST. This finding indicates that some traditional means of studying GMST variability (e.g., investigating preindustrial control runs or paleo-reconstructions of past variability) may be of limited utility for surmising information on the behavior of unforced GMST variability in a warmer climate.

Methods

Removal of model drift

All GFDL model data was detrended at the grid level with Empirical Mode Decomposition (EMD)[50,51], preventing nonphysical model drift from contaminating our analysis of variability.

Low-frequency Variability

We define the low-frequency component of variability using a 15-year lowess smooth[52] of a given time series. The conclusions of this study are unaltered when using a different filter (15-year running mean) and/or a different timescale (25 years).

Preindustrial vs. 2×CO₂ runs of the coupled GFDL CM3 model

GFDL CM3 is a coupled climate model with dynamic ocean, atmosphere, sea ice[53] and land[54,55] components[56–58]. The ocean model has a 1° tripolar 360×200 horizontal resolution, with 50 levels in the vertical[53]. The atmospheric model utilizes a 200 km horizontal resolution (C48L48) with 48 vertical levels up to 0.01 hPa[57]. The coupled model features interactive aerosol[59] and atmospheric chemistry[60] but does not simulate ocean biogeochemistry or ice sheet dynamics. We investigate changes in unforced variability between GFDL CM3's preindustrial control run and a run that has experienced a doubling of CO_2 from preindustrial values (1%/year) and has reached a new equilibrium state. We use the last 860 years of each run in order to ensure that the models were near equilibration. This meant that we omitted the first 220 years from the 1080-year preindustrial control run and the first 1,920 years from the 2,780 year 1%/year 2×CO₂ run, the latter so as not to include the transient warming phase and the subsequent slow equilibration to the new boundary conditions.

Atlantic Multidecadal Oscillation (AMO)

We define the AMO as the low-frequency component of the spatially weighted mean sea surface temperature between 7.5°W and 75°W and 0 and 65°N in the Atlantic Ocean.

Current SST vs. uniform +4K SST of the GFDL AM3 model

In order to isolate the role of atmospheric/surface process from the role ocean-atmosphere-sea ice processes, we conduct an experiment set where the atmospheric component of GFDL

CM3 (AM3) is forced by annually repeating climatological seasonal cycles of SSTs and sea ice (Fig. 4c and 4d). We compare a run forced with a climatological seasonal cycle of SSTs and sea ice[61] repeated annually to an identical run but with a uniform +4K increase of SSTs. In the +4K SST run, sea ice and vegetation were held constant. We investigate 200 years of variability in this experiment set. Note that GMST change in the uniform SST warming run (4.6K) is very similar to the magnitude of the GMST change between the preindustrial control and $2 \times CO_2$ coupled model runs (4.8K).

Change in unforced variability with warming in CMIP5 runs

The CMIP5 experiment design did not include equilibrated runs under a $2 \times CO_2$ condition and thus it was impossible to directly compare results between the GFDL CM3 experiment and other CMIP5 models. However, as a substitution for a direct comparison, we investigate how unforced low frequency variability changed in fully coupled CMIP5 models between their preindustrial control runs (first 200 years) and the years 2200–2300 of their RCP8.5 runs. The post 2200-time period was selected because there is little change in radiative forcing thereafter[62]. However, models are not equilibrated in the year 2200. Thus, in order to isolate unforced variability from forced variability, we regress-out the multi-model mean of a given variable's response at the grid level. Both the preindustrial control and RCP8.5 time periods were also subjected to detrending using Empirical Mode Decomposition to ensure time series were stationary priory to further analysis[50,51]. Nine CMIP5 models were available (with our required variables) with both preindustrial control and post 2200 RCP8.5 data archived (Supplementary Table 1).

Components of the top-of-atmosphere (TOA) net anomalous energy imbalance (↓N)

The net anomalous TOA energy imbalance, ↓N (Wm^{-2}), can be decomposed into four linearly additive components (↓N = [↓clear SW]+[↓clear LW]+[↓cloud SW]+[↓cloud LW])[63], where

$$\downarrow clear\ SW = [\downarrow SW - \uparrow SW_{clearsky}], \quad (1)$$

$$\downarrow clear\ LW = [- \uparrow LW_{clearsky}], \quad (2)$$

$$\downarrow cloud\ SW = [\downarrow SW - \uparrow SW_{allsky}] - [\downarrow SW - \uparrow SW_{clearsky}] = \uparrow SW_{clearsky} - \uparrow SW_{allsky} \quad (5)$$

$$\downarrow cloud\ LW = [- \uparrow LW_{allsky}] - [- \uparrow LW_{clearsky}] = \uparrow LW_{clearsky} - \uparrow LW_{allsky}. \quad (3)$$

Clear SW is the clear-sky shortwave component, clear LW is the clear-sky longwave component, cloud SW is the shortwave cloud radiative effect and cloud LW is the longwave cloud radiative effect.

Surface energy budget

The surface energy budget is defined in the typical way,

$$\uparrow Q = [\uparrow LE] + [\uparrow LH] + [\uparrow SW - \downarrow SW] + [\uparrow LW - \downarrow LW]. \quad (4)$$

In Figure 4, $\downarrow R_s$ is the downward oriented net radiative imbalance,

$$\downarrow R_s = [\downarrow SW - \uparrow SW] + [\downarrow LW - \uparrow LW]. \quad (5)$$

Confidence intervals for cross-regressions of Figure 2

In order to create the confidence intervals for the cross-regression coefficients shown in Figure 2, we used the Monte Carlo method described in the steps below:

1. At each time lag, AR(2) noise models were fit to both sub-samples of the time series under consideration using Akaike Information Criterion (AIK).

2. 10,000 synthetic time series were created for each of the two input samples.

3. All time series were smoothed using a 15-year lowess filter.

4. 10,000 regressions coefficients were calculated between the two groups of synthetic time series.

5. The 5th/95th percentile range of the regression coefficients was used as the range of the confidence interval.

Statistical significance of changes in local regression coefficients against GMST in Figure 3

In order to identify statistically significant changes in the regression coefficients against GMST between GFDL CM3's $2 \times CO_2$ and preindustrial control runs (Fig. 3), we used the Monte Carlo method described in the steps below:

1. AR(2) noise models were fit to both sets of time series under consideration for both runs (4 noise models in total) using Akaike Information Criterion (AIK).

2. 10,000 synthetic time series were created for each of the two input time series for each run (40,000 times series in total).

3. Time series were smoothed using a 15-year lowess filter.

4. 10,000 regression coefficients were calculated between the two time series for each run (20,000 regression coefficients in total).

5. A distribution of the difference between the regression coefficients was created.

6. The 5th and 95th percentiles of the difference distribution were noted.

7. If the measured difference in the regression coefficients was less than the 5th percentile or greater than the 95th percentile of the synthetic distribution, that difference was deemed to be significantly significant.

Error bars in Fig. 4b and 4d

Figs. 4b and 4d display standard errors of the mean differences between the model runs for a number of variables. These standard errors were calculated so that they accounted for spatial autocorrelation in the following way:

1. For a given variable (e.g., sensible heat flux), the map of the difference between the two runs was considered.

2. At each latitude between 70°N and 70°S, the decorrelation length scale in the zonal direction was computed. The decorrelation length scale was defined as the number of grid points that it took for the spatial autocorrelation function to drop below 1/e.

3. The map-mean decorrelation length scale was calculated by averaging together the zonal decorrelation length scales with cosine weights.

4. The effective number of independent grid points on the map (N_{eff}) was then calculated as the original number of grid points divided by the map-mean decorrelation length scale.

5. N_{eff} was then used in the calculation of the standard error.

Data availability

The CMIP5 data used for this study can be downloaded at http://cmip-pcmdi.llnl.gov/cmip5/data_portal.html and the GFDL model data can be downloaded at http://nomads.gfdl.noaa.gov:8080/DataPortal/cmip5.jsp. Other data that support the findings of this study are available from the corresponding author upon request.

Supplementary Material

Refer to Web version on PubMed Central for supplementary material.

Acknowledgments

References

1. Bindoff, NL., Stott, PA., AchutaRao, KM., Allen, MR., Gillett, N., Gutzler, D., Hansingo, K., Hegerl, G., Hu, Y., Jain, S., Mokhov, II., Overland, J., Perlwitz, J., Sebbari, R., Zhang, X. Climate Change 2013: The Physical Science Basis. Cambridge University Press; Cambridge, United Kingdom and New York, NY, USA: 2013. Detection and Attribution of Climate Change: from Global to Regional.

2. Hawkins E, Sutton R. The Potential to Narrow Uncertainty in Regional Climate Predictions. Bulletin of the American Meteorological Society. 2009; 90:1095–1107. DOI: 10.1175/2009BAMS2607.1

3. Meehl GA, et al. Decadal Prediction. Bulletin of the American Meteorological Society. 2009; 90:1467–1485. DOI: 10.1175/2009BAMS2778.1

4. Hasselmann K. Stochastic climate models Part I. Theory. Tellus. 1976; 28:473–485. DOI: 10.1111/j.2153-3490.1976.tb00696.x

5. Brown PT, Li W, Xie S-P. Regions of significant influence on unforced global mean surface air temperature variability in climate models. Journal of Geophysical Research: Atmospheres. 2015 2014JD022576.

6. Brown PT, Li W, Li L, Ming Y. Top-of-Atmosphere Radiative Contribution to Unforced Decadal Global Temperature Variability in Climate Models. Geophysical Research Letters. 2014 2014GL060625.

7. Knutson TR, Zhang R, Horowitz LW. Prospects for a prolonged slowdown in global warming in the early 21st century. Nature Communications. 2016; 7:13676.

8. Huber M, Knutti R. Natural variability, radiative forcing and climate response in the recent hiatus reconciled. Nature Geosci. 2014

9. Roberts CD, Palmer MD, McNeall D, Collins M. Quantifying the likelihood of a continued hiatus in global warming. Nature Clim Change. 2015; 5:337–342. DOI: 10.1038/nclimate2531

10. Middlemas E, Clement AMY. Spatial patterns and frequency of unforced decadal-scale changes in global mean surface temperature in climate models. J Clim. 2016

11. Brown PT, Li W, Cordero EC, Mauget SA. Comparing the model-simulated global warming signal to observations using empirical estimates of unforced noise. Sci Rep. 2015; 5

12. Schurer AP, Hegerl GC, Mann ME, Tett SFB, Phipps SJ. Separating Forced from Chaotic Climate Variability over the Past Millennium. Journal of Climate. 2013; 26:6954–6973. DOI: 10.1175/JCLI-D-12-00826.1

13. Crowley TJ, Obrochta SP, Liu J. Recent global temperature "plateau" in the context of a new proxy reconstruction. Earth's Future. 2014; 2:281–294. DOI: 10.1002/2013EF000216

14. Jones GS, Stott PA, Christidis N. Attribution of observed historical near-surface temperature variations to anthropogenic and natural causes using CMIP5 simulations. Journal of Geophysical Research: Atmospheres. 2013; 118:4001–4024. DOI: 10.1002/jgrd.50239

15. Crowley TJ. Causes of Climate Change Over the Past 1000 Years. Science. 2000; 289:270–277. DOI: 10.1126/science.289.5477.270 [PubMed: 10894770]

16. Mann ME, Steinman BA, Miller SK. On Forced Temperature Changes, Internal Variability and the AMO. Geophysical Research Letters. 2014 2014GL059233.

17. Muller RA, et al. Decadal variations in the global atmospheric land temperatures. Journal of Geophysical Research: Atmospheres. 2013; 118:5280–5286. DOI: 10.1002/jgrd.50458

18. Meehl GA, Teng H, Arblaster JM. Climate model simulations of the observed early-2000s hiatus of global warming. Nature Clim Change. 2014; 4:898–902. DOI: 10.1038/nclimate2357

19. Santer BD, et al. Separating signal and noise in atmospheric temperature changes: The importance of timescale. Journal of Geophysical Research: Atmospheres. 2011; 116:D22105.

20. Risbey JS, et al. Well-estimated global surface warming in climate projections selected for ENSO phase. Nature Clim Change. 2014

21. Maher N, Gupta AS, England MH. Drivers of decadal hiatus periods in the 20th and 21st centuries. Geophysical Research Letters. 2014; 41:5978–5986. DOI: 10.1002/2014GL060527

22. Collins, M., Knutti, R., Arblaster, J., Dufresne, J-L., Fichefet, T., Friedlingstein, P., Gao, X., Gutowski, WJ., Johns, T., Krinner, G., Shongwe, M., Tebaldi, C., Weaver, AJ., Wehner, M.

Climate Change 2013: The Physical Science Basis. Contribution of Working Group I to the Fifth Assessment Report of the Intergovernmental Panel on Climate Change. Cambridge University Press; Cambridge, United Kingdom and New York, NY, USA: 2013. Long-term Climate Change: Projections, Commitments and Irreversibility.

23. de Lavergne C, Palter JB, Galbraith ED, Bernardello R, Marinov I. Cessation of deep convection in the open Southern Ocean under anthropogenic climate change. Nature Clim Change. 2014; 4:278–282. DOI: 10.1038/nclimate2132

24. Joshi MM, Gregory JM, Webb MJ, Sexton DMH, Johns TC. Mechanisms for the land/sea warming contrast exhibited by simulations of climate change. Climate Dynamics. 2007; 30:455–465. DOI: 10.1007/s00382-007-0306-1

25. Huntingford C, Jones PD, Livina VN, Lenton TM, Cox PM. No increase in global temperature variability despite changing regional patterns. Nature. 2013; 500:327–330. DOI: 10.1038/nature12310 [PubMed: 23883935]

26. Räisänen J. CO2-Induced Changes in Interannual Temperature and Precipitation Variability in 19 CMIP2 Experiments. Journal of Climate. 2002; 15:2395–2411. DOI: 10.1175/1520-0442(2002)015<2395:CICIIT>2.0.CO;2

27. Boer JG, Flato G, Ramsden D. A transient climate change simulation with greenhouse gas and aerosol forcing: projected climate to the twenty-first century. Climate Dynamics. 16:427–450. DOI: 10.1007/s003820050338

28. Meehl GA, Wheeler M, Washington WM. Low-frequency variability and CO2 transient climate change. Part 3. Intermonthly and interannual variability. Climate Dynamics. 10:277–303. DOI: 10.1007/bf00228028

29. Rind D, Goldberg R, Ruedy R. Change in climate variability in the 21st century. Climatic Change. 14:5–37. DOI: 10.1007/bf00140173

30. Sakai D, Itoh H, Yukimoto S. Changes in the Interannual Surface Air Temperature Variability in the Northern Hemisphere in Response to Global Warming. Journal of the Meteorological Society of Japan Ser II. 2009; 87:721–737. DOI: 10.2151/jmsj.87.721

31. Boer GJ. Changes in Interannual Variability and Decadal Potential Predictability under Global Warming. Journal of Climate. 2009; 22:3098–3109. DOI: 10.1175/2008JCLI2835.1

32. Stouffer RJ, Wetherald RT. Changes of Variability in Response to Increasing Greenhouse Gases. Part I: Temperature. Journal of Climate. 2007; 20:5455–5467. DOI: 10.1175/2007JCLI1384.1

33. Taylor KE, Stouffer RJ, Meehl GA. An Overview of CMIP5 and the Experiment Design. Bulletin of the American Meteorological Society. 2011; 93:485–498. DOI: 10.1175/BAMS-D-11-00094.1

34. Cleveland WS. Robust Locally Weighted Regression and Smoothing Scatterplots. Journal of the American Statistical Association. 1979; 74:829–836. DOI: 10.1080/01621459.1979.10481038

35. England MH, et al. Recent intensification of wind-driven circulation in the Pacific and the ongoing warming hiatus. Nature Clim Change. 2014

36. Chen X, Tung K-K. Varying planetary heat sink led to global-warming slowdown and acceleration. Science. 2014; 345:897–903. DOI: 10.1126/science.1254937 [PubMed: 25146282]

37. Drijfhout SS, et al. Surface warming hiatus caused by increased heat uptake across multiple ocean basins. Geophysical Research Letters. 2014; 41:7868–7874. DOI: 10.1002/2014GL061456

38. Meehl GA, Hu A, Arblaster JM, Fasullo J, Trenberth KE. Externally Forced and Internally Generated Decadal Climate Variability Associated with the Interdecadal Pacific Oscillation. Journal of Climate. 2013; 26:7298–7310. DOI: 10.1175/JCLI-D-12-00548.1

39. Xie S-P, Kosaka Y, Okumura YM. Distinct energy budgets for anthropogenic and natural changes during global warming hiatus. Nature Geosci. 2016; 9:29–33. DOI: 10.1038/ngeo2581

40. Hedemann C, Mauritsen T, Jungclaus J, Marotzke J. The subtle origins of surface-warming hiatuses. Nature Clim Change. 2017; 7:336–339. DOI: 10.1038/nclimate3274

41. Pedro JB, et al. Southern Ocean deep convection as a driver of Antarctic warming events. Geophysical Research Letters. 2016; 43:2192–2199. DOI: 10.1002/2016GL067861

42. Behrens E, et al. Southern Ocean deep convection in global climate models: A driver for variability of subpolar gyres and Drake Passage transport on decadal timescales. Journal of Geophysical Research: Oceans. 2016

43. Martin T, Park W, Latif M. Multi-centennial variability controlled by Southern Ocean convection in the Kiel Climate Model. Climate Dynamics. 2013; 40:2005–2022. DOI: 10.1007/s00382-012-1586-7

44. Brown PT, Lozier MS, Zhang R, Li W. The necessity of cloud feedback for a basin-scale Atlantic Multidecadal Oscillation. Under revision - Geophysical Research Letters. 2016

45. Brown PT, Li W, Jiang JH, Su H. Spread in the magnitude of climate model interdecadal global temperature variability traced to disagreements over high-latitude oceans. Geophysical Research Letters. 2016; 43(12):543–512. 549. DOI: 10.1002/2016GL071442

46. Sherwood S, Fu Q. A Drier Future? Science. 2014; 343:737–739. DOI: 10.1126/science.1247620 [PubMed: 24531959]

47. Byrne MP, O'Gorman PA. Link between land-ocean warming contrast and surface relative humidities in simulations with coupled climate models. Geophysical Research Letters. 2013; 40:5223–5227. DOI: 10.1002/grl.50971

48. Berg A, et al. Land-atmosphere feedbacks amplify aridity increase over land under global warming. Nature Clim Change. 2016

49. Flato, G., Marotzke, J., Abiodun, B., Braconnot, P., Chou, SC., Collins, W., Cox, P., Driouech, F., Emori, S., Eyring, V., Forest, C., Gleckler, P., Guilyardi, E., Jakob, C., Kattsov, V., Reason, C., Rummukainen, M. Climate Change 2013: The Physical Science Basis Contribution of Working Group I to the Fifth Assessment Report of the Intergovernmental Panel on Climate Change. Cambridge University Press; Cambridge, United Kingdom and New York, NY, USA: 2013. Evaluation of Climate Models.

50. Huang NE, et al. The empirical mode decomposition and the Hilbert spectrum for nonlinear and non-stationary time series analysis. Proceedings of the Royal Society of London Series A: Mathematical, Physical and Engineering Sciences. 1998; 454:903–995. DOI: 10.1098/rspa.1998.0193

51. Wu Z, Huang NE, Long SR, Peng C-K. On the trend, detrending, and variability of nonlinear and nonstationary time series. Proceedings of the National Academy of Sciences. 2007; 104:14889–14894. DOI: 10.1073/pnas.0701020104

52. Cleveland WS. Robust Locally Weighted Regression and Smoothing Scatterplots. Journal of the American Statistical Association. 1979; 74:829–836. DOI: 10.1080/01621459.1979.10481038

53. Griffies SM, Greatbatch RJ. Physical processes that impact the evolution of global mean sea level in ocean climate models. Ocean Modelling. 2012; 51:37–72. DOI: 10.1016/j.ocemod.2012.04.003

54. Milly PCD, Shmakin AB. Global Modeling of Land Water and Energy Balances. Part I: The Land Dynamics (LaD) Model. Journal of Hydrometeorology. 2002; 3:283–299. DOI: 10.1175/1525-7541(2002)003<0283:GMOLWA>2.0.CO;2

55. Shevliakova E, et al. Carbon cycling under 300 years of land use change: Importance of the secondary vegetation sink. Global Biogeochemical Cycles. 2009:23.

56. Griffies SM, et al. The GFDL CM3 Coupled Climate Model: Characteristics of the Ocean and Sea Ice Simulations. Journal of Climate. 2011; 24:3520–3544. DOI: 10.1175/2011JCLI3964.1

57. Donner LJ, et al. The Dynamical Core, Physical Parameterizations, and Basic Simulation Characteristics of the Atmospheric Component AM3 of the GFDL Global Coupled Model CM3. Journal of Climate. 2011; 24:3484–3519. DOI: 10.1175/2011JCLI3955.1

58. Delworth TL, et al. GFDL's CM2 Global Coupled Climate Models. Part I: Formulation and Simulation Characteristics. Journal of Climate. 2006; 19:643–674. DOI: 10.1175/JCLI3629.1

59. Levy H, et al. The roles of aerosol direct and indirect effects in past and future climate change. Journal of Geophysical Research: Atmospheres. 2013; 118:4521–4532. DOI: 10.1002/jgrd.50192

60. Austin J, Wilson RJ. Ensemble simulations of the decline and recovery of stratospheric ozone. Journal of Geophysical Research: Atmospheres. 2006; 111 n/a–n/a.

61. Hurrell JW, Hack JJ, Shea D, Caron JM, Rosinski J. A New Sea Surface Temperature and Sea Ice Boundary Dataset for the Community Atmosphere Model. Journal of Climate. 2008; 21:5145–5153. DOI: 10.1175/2008JCLI2292.1

62. Meinshausen M, et al. The RCP greenhouse gas concentrations and their extensions from 1765 to 2300. Climatic Change. 2011; 109:213–241. DOI: 10.1007/s10584-011-0156-z

63. Ramanathan V, et al. Cloud-Radiative Forcing and Climate: Results from the Earth Radiation Budget Experiment. Science. 1989; 243:57–63. DOI: 10.1126/science.243.4887.57 [PubMed: 17780422]
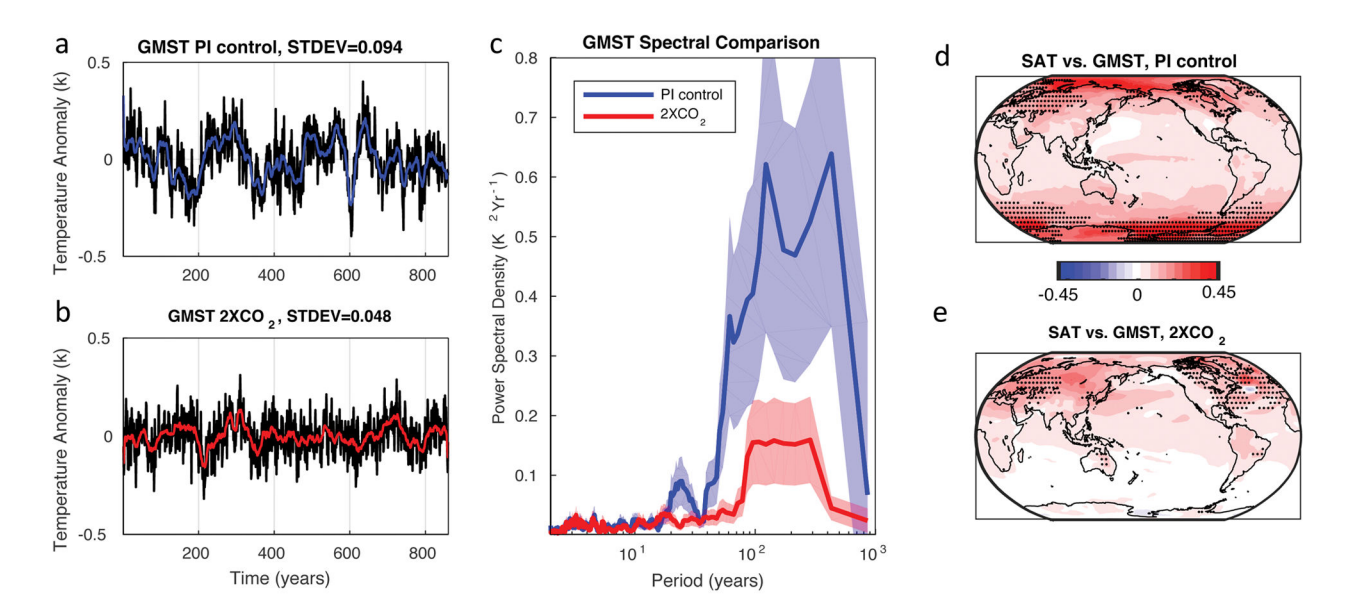
Figure 1. Magnitude and geographic origin of GMST variability in the GFDL CM3 preindustrial control and 2×CO2 runs

a, Annual mean time series of GMST variability (black) in the preindustrial control run with the low-frequency component (15-year Lowess smooth) shown in blue. **b**, As in (**a**) but in the 2×CO$_2$ run. The time series in (**a**) and (**b**) are displayed as anomalies relative to their own GMST climatology but this climatology is 4.8K warmer in the 2×CO$_2$ run. **c**, Power spectral density (smoothed with a 9-period running mean) of the two time series shown in **a** (blue) and **b** (red) with 1σ confidence intervals displayed. **d**, Local low-frequency SAT variability regressed against the standard deviation of low-frequency GMST variability in the preindustrial control run. **e**, As in (**d**) but for the 2×CO2 run. Stippling in (**d**) and (**e**) represent Regions of Significant Influence[5] which highlight the locations (and by proxy modes of variability) that have the most influence on GMST variability (see main text, and ref (5) for more details).
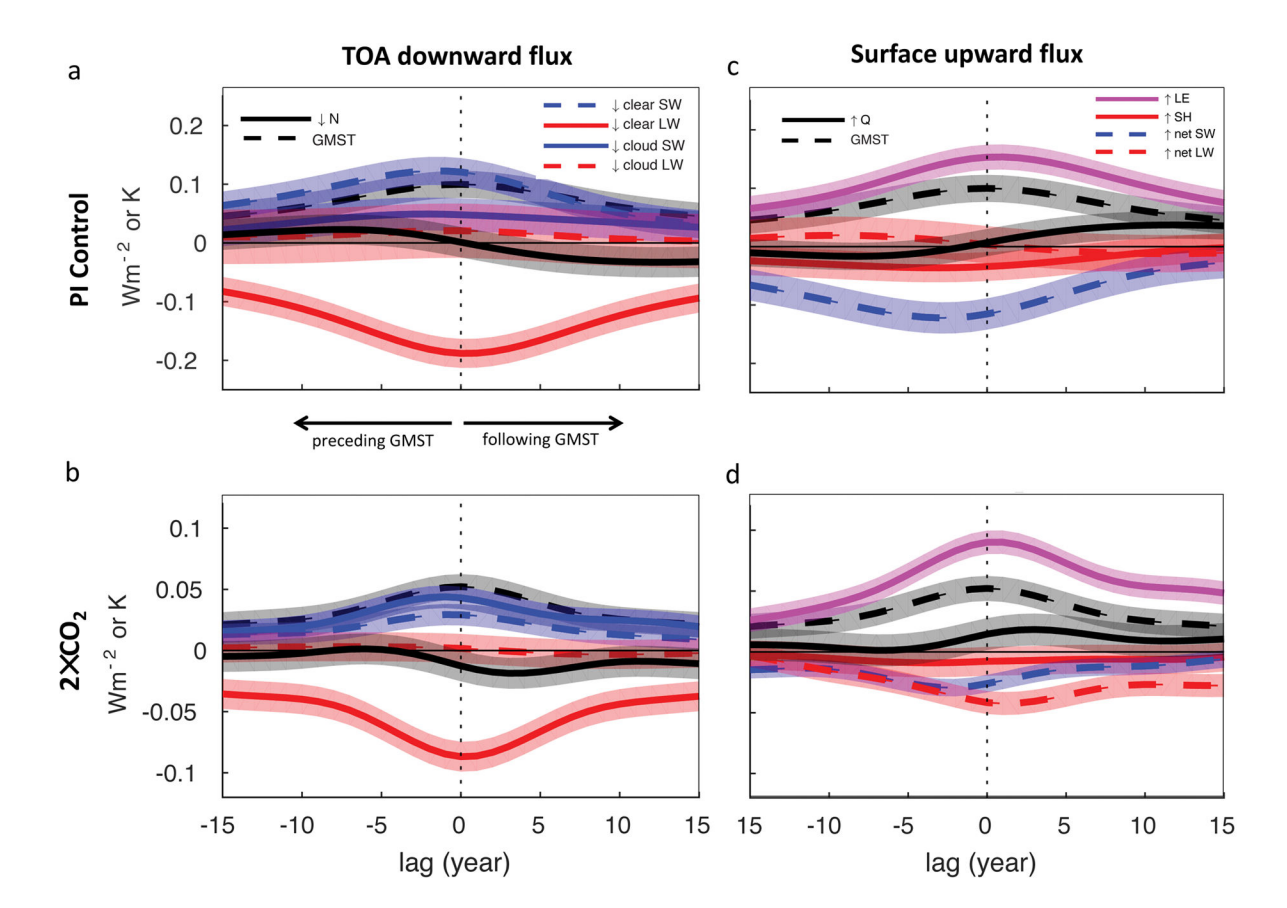
Figure 2. Relationship between GMST and the TOA and surface energy budgets in the GFDL CM3 preindustrial control and 2×CO₂ runs

Cross regression (lagged linear least-squares regression coefficients) between the low-frequency component of the labeled variables and the standard deviation of the low-frequency component of GMST. TOA components are shown in (a, b) and surface components are shown in (c, d) for the preindustrial control run (a, c) and the 2×CO2 run (b, d). Note that the Y axis spans a smaller range in the 2×CO2 run (b, d) indicating that the magnitude of variability tends to be smaller. TOA components (a, b) are positive down while surface components (c, d) are positive up. The dashed black line is GMST regressed against normalized GMST. The thickness of the confidence intervals represents the 2σ range of regression coefficients between time series with similar autocorrelation but with no relation to one and other. See Methods section for further details on the calculation of the confidence intervals.
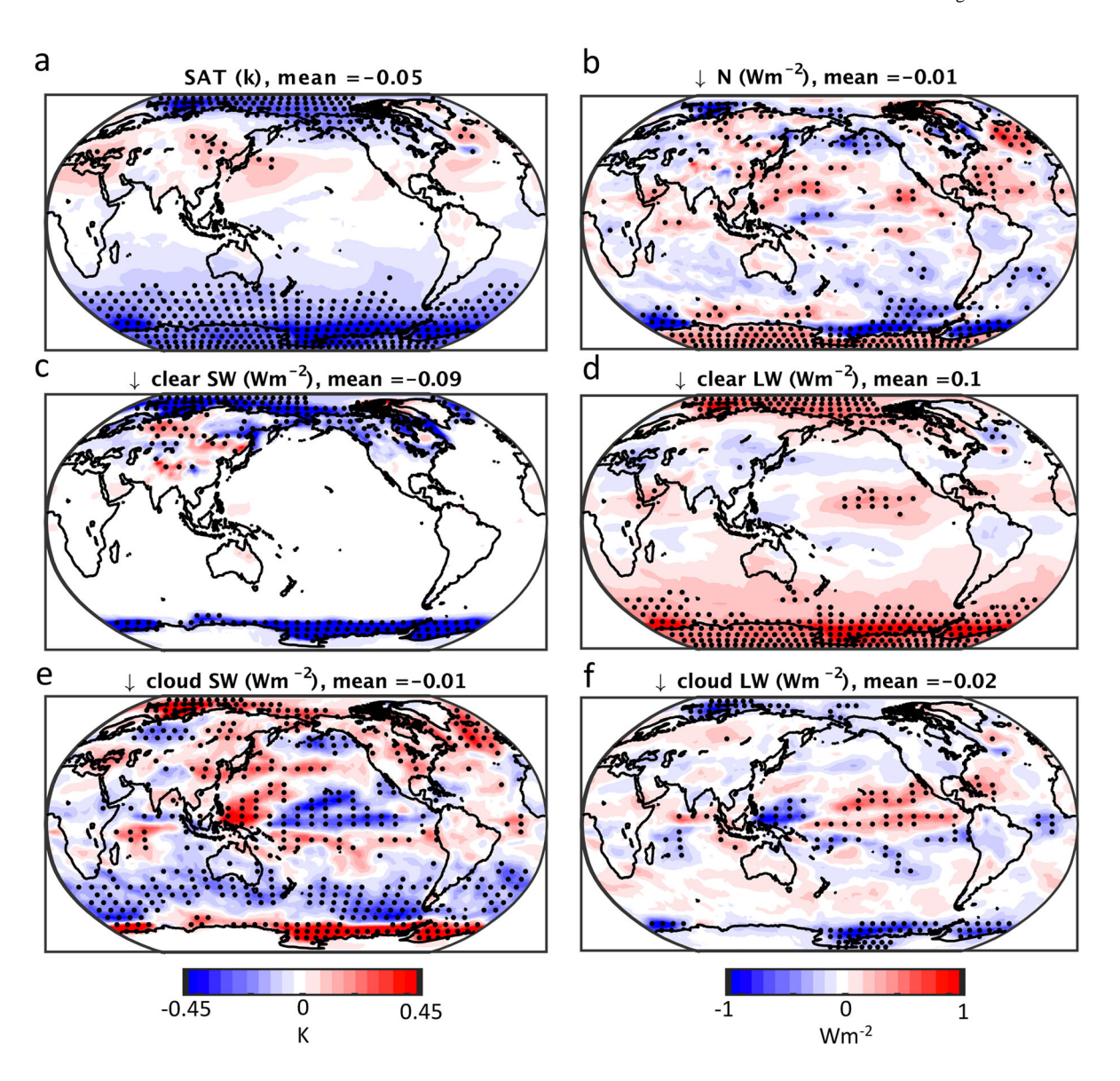
a   **SAT (k), mean =−0.05**

b   **↓ N (Wm^{-2}), mean =−0.01**

c   **↓ clear SW (Wm^{-2}), mean =−0.09**

d   **↓ clear LW (Wm^{-2}), mean =0.1**

e   **↓ cloud SW (Wm^{-2}), mean =−0.01**

f   **↓ cloud LW (Wm^{-2}), mean =−0.02**

-0.45   0   0.45
K

-1   0   1
Wm^{-2}

Figure 3. Change in the TOA energy budget contribution to GMST variability between the GFDL CM3 preindustrial control and 2×CO2 runs

Change in the local regression against the standard deviation of GMST for surface air temperature (a), net top of atmosphere radiative imbalance (b), clear sky shortwave top of atmosphere radiative imbalance (c), clear-sky longwave top of atmosphere radiative imbalance (d), shortwave cloud radiative effect (e) and longwave cloud radiative effect (f). The global mean value of the variable is displayed for each panel. Stippling in panels represents statistically significant differences in regression coefficients calculated using a Monte Carlo technique (see Methods).
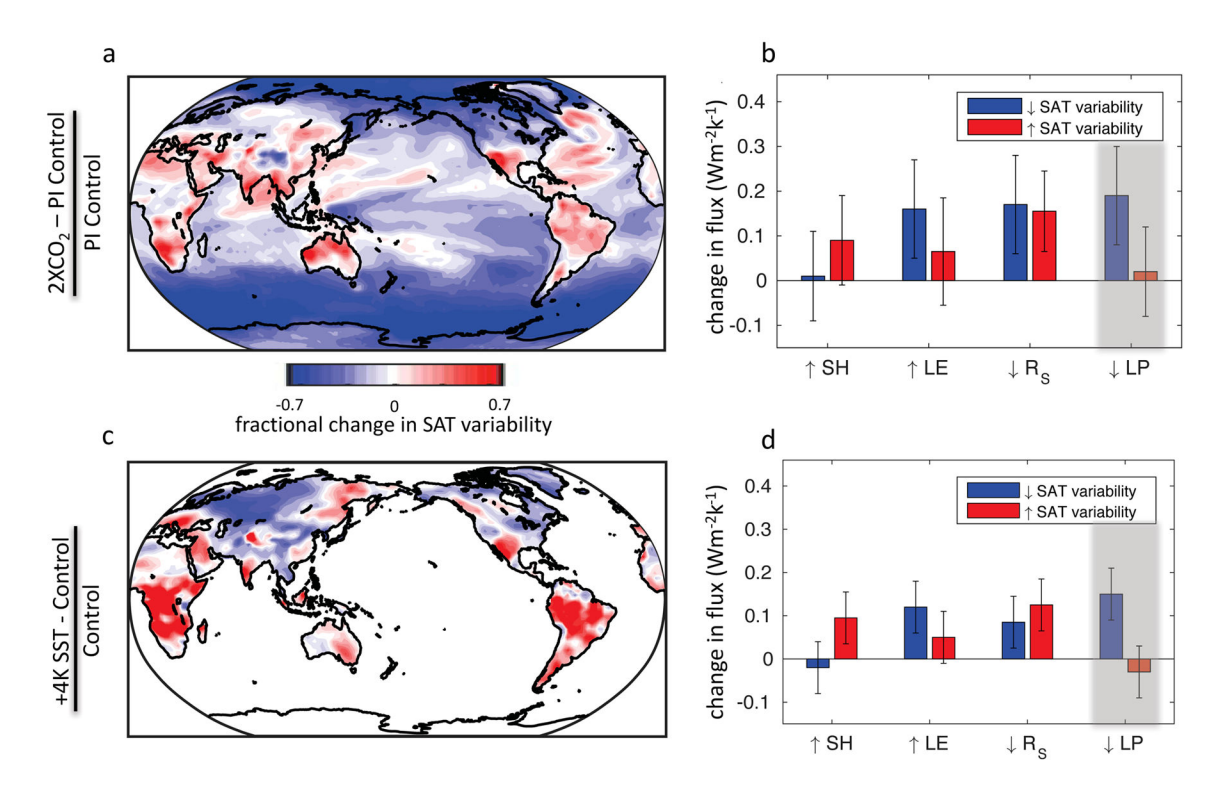
Figure 4. Change in local temperature variability

a, Fractional change in the local temporal standard deviation of low-frequency SAT between the GFDL CM3 preindustrial control and $2\times CO_2$ runs (unitless). **c**, As in (a) but the fractional change between the GFDL AM3 observed SST run and +4K SST run (see Methods). **b**, Change in the climatological energy flux ($Wm^{-2}K^{-1}$) over land regions that experienced an increase in SAT variability (red) and land regions that experienced a decrease in SAT variability (blue) between the GFDL CM3 preindustrial control and $2\times CO_2$ runs. **d**, As in **b** but change between the GFDL AM3 +4K SST and observed SST run. In b and d ↑SH is upward sensible heat flux, ↑LE is upward latent heat flux, $\downarrow R_s$ is the net downward radiation, and ↓LP is the latent heat of vaporization times the precipitation. ↓LP is shaded grey to indicate that it is not formally part of the energy budget but is used here as a proxy for water availability. The vertical error bars represent the standard error across all grid points accounting for spatial autocorrelation (see Methods).